Phase diagram of tobacco mosaic virus solutions

Hartmut Graf and Hartmut Löwen*
Institut für Theoretische Physik II, Heinrich-Heine-Universität Düsseldorf, Universitätsstraße 1, D-40225 Düsseldorf, Germany
(Received 13 July 1998)

The phase behavior of an aqueous suspension of rodlike tobacco mosaic viruses is investigated theoretically as a function of the virus density and the concentration of added salt. The total free energy involves ''volume terms'' from the microscopic counter- and co-ions and an effective pair interaction between the colloidal rods described by a Yukawa-segment model according to linear screening theory. Within a thermodynamic perturbation approach, the short-range repulsion between the rods is mapped onto a reference system of effective hard spherocylinders. The free energy of the spherocylinder system is gained from combining a cell model with scaled particle theory, which yields a reasonable phase diagram. The remaining long-range interaction is treated within a mean-field approximation. As a result we find stable fluid, nematic, and smectic phases as well as *AAA*- and *ABC*-stacked crystals. For increasing salt concentration at fixed rod concentration, there is a nematic reentrant transition. We finally discuss our results in view of experimental data.
[S1063-651X(99)01302-1]

PACS number(s): 82.70.Dd, 64.70.Md

I. INTRODUCTION

In the 1930s the existence of colloidal liquid crystalline phases was detected in aqueous suspensions of the *tobacco mosaic virus* (TMV): A phase separation into a (thinner) optical isotropic and a (thicker) birefringent phase was observed when the virus concentration exceeded 2% [1]. Subsequently, higher ordered liquid-crystalline phases were discovered for samples under different conditions: Layered structures [2–4] were proved to be either a colloidal crystal [5] or a smectic phase [6], depending on the ionic strength. For highly deionized samples the structure is still controversial; here some evidence for a columnar phase has been reported [7]. Still the full phase diagram of an aqueous TMV suspension as a function of its density and the ionic strength is not known.

Over other rodlike colloidal samples, e.g., the fd virus [8–10] or Boehmite rods [11,12], the TMV has the important advantage that it is practically rigid and monodisperse, which facilitates a theoretical description with an effective orientation-dependent pair interaction. The simplest model system of a lyotropic colloidal liquid crystal is that of *hard spherocylinders* (HSCs) with a pure excluded volume interaction. Within this model, Onsager [13] explained the isotropic-nematic transition for large aspect ratios p of the HSC. Although the model is quite simple and governed by only two parameters, namely, the particle density and p, it is only recently that the full phase diagram was explored by computer simulation; see Ref. [14]. As the TMV is charged stabilized, the interaction between two rods will be long ranged (at least for strongly deionized samples). The simplest approach to include these long-ranged interactions is to describe them approximately in an effective diameter as already done by Onsager. This method had been expanded by Stroobants *et al.* [15], who included the twisting effect, i.e., nearly touching charged rods tend to orient perpendicular to minimize their potential energy.

In this paper we start from the primitive model of strongly asymmetric electrolytes (charged colloidal rods, counterions, and co-ions). Linear screening theory results in an effective Yukawa-segment model describing the interaction between two rods plus additional ''volume terms'' comprising the free energy of the counter- and co-ions as obtained for spherical macro-ions recently by van Roij and Hansen [16]; see also [17]. These terms are particularly important for low salt concentrations. The Yukawa-segment interaction is split into a short-ranged and a long-ranged part according to standard thermodynamic perturbation theory. Using the system of hard spherocylinders as a reference system for the short-ranged part and describing the long-ranged part on a mean-field level, we obtain the free energies in the various liquid-crystalline phases and the overall phase diagram. We finally remark that Han and Herzfeld [18] recently proposed a similar strategy, deriving the effective shape of a HSC reference system from a self-consistent interplay between the reference system and a mean-field description. In this work, however, only low ordered phases were under consideration and the ''volume terms'' have been neglected.

The paper is organized as follows. Free energies of the different phases in the hard spherocylinder model are considered in Sec. II. We combine a cell model with a scaled particle theory and find that the resulting phase diagram compares reasonably well with the computer simulation data. In Sec. III we introduce a perturbation scheme for charged rodlike colloidal suspensions and show how to apply it to various liquid-crystalline phases. Results for the phase diagram are presented in Sec. IV. We present in Sec. V a brief comparison of our theoretical results with available experimental data. We conclude in Sec. VI.

II. CELL MODEL THEORY FOR THE PHASE BEHAVIOR OF HARD SPHEROCYLINDERS

A. Basic features of the model

The shape of the HSC contains a cylindric part capped with two hemispheres at the ends such that it is characterized

*Also at Institut für Festkörperforschung, Forschungszentrum Jülich, D-52425 Jülich, Germany.

by a total length L and a width D. The anisotropy of the particle is measured by the aspect ratio $p=L/D$. In general, its center-of-mass position is denoted $\vec{r}$ and its orientation is described by a unit vector $\vec{\omega}$ pointing along the cylindrical axis. A system of N HSCs is one of the simplest models for rodlike particles since k_BT simply sets the energy scale. Hence there are only two independent parameters, namely, the aspect ratio p and the cylinder number density $\rho=N/V$, where V is the system volume. This density can conveniently be expressed in terms of the close-packed density

$$\rho_{\mathrm{CP}}=\frac{2}{(\sqrt{2}+\sqrt{3}p)\ D^3}. \tag{1}$$

Two limiting cases are of special interest. First, for $p=0$, the hard sphere model is recovered. In the opposite so-called Onsager limit of infinitely long rods $p\to\infty$ one can asymptotically calculate the isotropic-nematic phase transition analytically.

The phase diagram of HSCs for all aspect ratios has only very recently been explored by Monte Carlo simulations [14]. Previously, simulation results had been available only for very few values of p [19–21], whereas analytic calculations, mainly based on density-functional methods, had been restricted to low-order phases [22–25]. In the rest of this section we present a simple theory, which accounts for the phase behavior of HSCs semiquantitatively, though with less numerical effort. A comparison with available Monte Carlo data [14] shows quite good agreement. Parts of this work were already published elsewhere [17].

B. Fundamental concepts of the theory

The basic ingredient to obtain the phase behavior is the reduced free energy per particle $f=\beta F/N$ in the different phases from which the pressure and the chemical potential can be derived. Here $1/\beta=k_BT$ is the thermal energy. The phase coexistence is then achieved by a usual common tangent construction to the free energies of the two coexisting phases. In order to access f, we shall either take known expressions or use a variational cell theory for the one-particle density $\rho^{(1)}(\vec{r},\vec{\omega})$ of the HSC.

The fundamental approximation for our treatment of the anisotropic particles is the factorization of translational (spatial) and orientational degrees of freedom. The orientational free energy f^{rot} describes ideal (i.e., noninteracting) rotators obeying a fixed orientational distribution $g(\vec{\omega})$, which is given explicitly below. Except for the fluid phase, where we use a scaled particle theory [26], we obtain the free energy of the translational degrees of freedom f^{spat} by mapping the system onto a substitute system of completely aligned particles with an effective shape. Thus we have $f=f^{\mathrm{rot}}+f^{\mathrm{spat}}$. Let us outline the different steps in more detail.

C. Handling the orientational degrees of freedom

The orientation distribution function $g(\vec{\omega})$ is assumed to be spatially invariant, being thus proportional to the spatial averaged one-particle density $\rho^{(1)}(\vec{r},\vec{\omega}):g(\vec{\omega})=N^{-1}\int d^3\vec{r}\,\rho^{(1)}(\vec{r},\vec{\omega})$. The quantity $g(\vec{\omega})$ measures the probability of the rods pointing in direction $\vec{\omega}$. We shall use $g(\vec{\omega})$ as a trial function, where the single variational parameter α describes the width of the orientation distribution around a given director $\vec{\omega}_0$. In particular, we use a Meier-Saupe form for $g(\vec{\omega})$, i.e.,

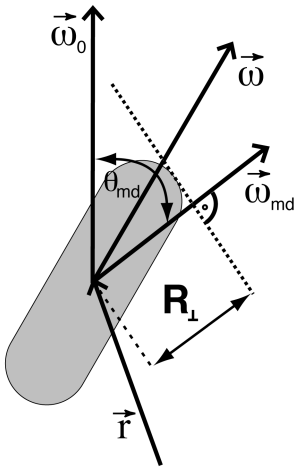

FIG. 1. Construction of the mean distance. The configuration parameters of the particle are given by the center-of-mass vector $\vec{r}$ and the unit vector $\vec{\omega}$ pointing in the direction of the particle. The nematic director is pointing along $\vec{\omega}_0$. The normal of the touching plane points in direction $\vec{\omega}_{\mathrm{MD}}$. Note that the mean distance $R_\perp$ is rotational invariant around the nematic director.

$$g(\vec{\omega})=\mathcal{N}^{-1}\exp[\alpha P_2(\vec{\omega}\cdot\vec{\omega}_0)], \tag{2}$$

where $P_2(x)=(3x^2-1)/2$ is the second Legendre polynomial and $\mathcal{N}$ is to guarantee correct normalization $\int_{S_2}g(\vec{\omega})d^2\vec{\omega}=1$. The integration with respect to the orientations is performed on the unit sphere S_2: $\int_{S_2}d^2\vec{\omega}=\int_0^{2\pi}d\phi\int_0^{\pi}\sin(\theta)d\theta=4\pi$. The rotational free energy thus reads

$$f^{\mathrm{rot}}=\int d^2\vec{\omega}\,g(\vec{\omega})\ln[g(\vec{\omega})]. \tag{3}$$

D. Mapping onto an effective oriented system

In the different phases, we map orientable particles onto effective oriented ones. Their effective shape is constructed as follows. First, let the center-of-mass position of a HSC be fixed and let $\vec{\omega}_0$ be the direction of the nematic director. We start from the convex envelope of all planes touching a spherocylinder pointing in direction $\vec{\omega}$. The shortest distance $R_\perp$ from the center-of-mass position to a plane in direction $\vec{\omega}_{\mathrm{MD}}$ touching the HSC (see Fig. 1) will be now averaged with respect to the orientation distribution function $g(\vec{\omega})$, which yields the mean distance

$$\overline{R}(\theta_{\mathrm{MD}},[g])=\frac{D}{2}+\frac{L}{2}\int_{S_2}d^2\vec{\omega}\,g(\vec{\omega})|(\vec{\omega}_{\mathrm{MD}}\cdot\vec{\omega})|. \tag{4}$$

The effective shape now is the Legendre transform of $\overline{R}$ with respect to θ_{MD}, defined by $\cos\theta_{\mathrm{MD}}=\vec{\omega}_0\cdot\vec{\omega}_{\mathrm{MD}}$. This construction embodies approximately orientational fluctuations in an average sense into the effective shape of a substitute hard body. It is instructive to consider two limiting cases. First, for fully aligned spherocylinders we have $g(\vec{\omega})=\delta(\vec{\omega}-\vec{\omega}_0)$ and the effective shape coincides with the original HSC shape. Second, for an isotropic distribution $g(\vec{\omega})=1/4\pi$, the effective shape is a sphere with the mean radius of curvature $R_{\mathrm{mean}}=D/2+L/4$ [27,26].

Except for the crystalline phases, we approximate the effective shape further as effective *aligned* hard spherocylinders with an effective diameter $D^*=2\overline{R}(\theta_{\mathrm{MD}}=\pi/2;[g])$ and an effective length $L^*=2\overline{R}(\theta_{\mathrm{MD}}=0;[g])-D^*$. In this substitute system we split the free energy stemming from the center-of-mass coordinates into a part describing the fluidlike dimensions and another one describing the solidlike dimensions. We treat the fluidlike dimensions with a scaled particle description, whereas for the solidlike dimension we use a cell model. For strictly aligned spherocylinders Taylor *et al.* [28] applied such a strategy to calculate the phase diagram. The *scaled particle theory* combines the probability of particle insertion with the pressure at a plane wall scaling between both expressions to derive an expression for the equation of state [26]. The basic idea for a *free volume theory* is to divide the space into equal compartments, each containing a single particle that moves there independent of the neighbor particles. The partition function factorizes by this assumption. Recall the case of hard spheres [29,30], where the configurational integral Q_N factorizes as

$$Q_N=\frac{1}{N!}\int_V d^3\vec{r}_1\cdots\int_V d^3\vec{r}_N e^{-\beta U_{\mathrm{pot}}^{\mathrm{HS}}(\vec{r}_1,\ldots,\vec{r}_N)} \leqslant\left[\int_{v_{\mathrm{free}}} d^3\vec{r}\right]^N=v_{\mathrm{free}}^N. \tag{5}$$

Here v_{free} is the free volume one particle can access within a single cell. For hard spheres the free energy obtained by the cell theory provides a strict upper bound to the real free energy. In our approach, however, this property is lost since we already did approximations.

Variational parameters, i.e., the width of the orientation distribution, distinguish the one-particle density fields in the various phases. To optimize the mapping, we therefore finally *minimize* the free energy with respect to these parameters. In the following, the whole strategy will be illustrated for the different liquid-crystalline phases.

E. Different phases in systems of hard spherocylinders

1. ABC crystal

Hard spheres are known to freeze in a face-centered-cubic crystal [31,32]. One obtains the corresponding structure of HSCs by stretching the fcc crystal along the 111 direction. The hexagonal layers of HSCs perpendicular to the director are then stacked as an ABC sequence. This structure is also the close-packed structure for HSCs.

The free energy of the system is obtained by a modified cell model: The basic assumption is that the free volume cell for the HSC with the effective shape has the same form as the one of hard spheres, being a rhombic dodecahedron. Its free volume v_{free}^{ABC} is given in Appendix A. Hence we obtain for the reduced free energy per particle in the ABC crystal

$$\tilde{f}_{ABC}(\alpha)=f^{\mathrm{rot}}(\alpha)-\ln[\Lambda^{-3}v_{\mathrm{free}}^{ABC}(\alpha)], \tag{6}$$

where α is the variational parameter for the orientational distribution and Λ is the thermal de Broglie wavelength. Our proposed cell model reduces for $p=0$ to the familiar hard-sphere cell model. In order to obtain the correct coexistence densities for the hard-sphere fluid-solid transition one therefore reduces the free energy by an empirical fit parameter $C_s=-1.8$ [33] to obtain

$$f_{ABC}=\tilde{f}_{ABC}+C_s. \tag{7}$$

The constant C_s is now used consistently for all aspect ratios in all solidlike phases, but not in the isotropic and nematic phases. We finally have to minimize the free energy with respect to the orientation distribution to optimize the mapping on the effective parallel particles.

2. Plastic crystal phase

In the plastic crystal phase, the center-of-mass coordinates are perfectly ordered on an fcc lattice while the orientation distribution is constant. By our construction of the effective size $\overline{R}$ for such a rotator solid, we obtain an effective hard sphere with radius $R_{\mathrm{mean}}=D/2+L/4$. The free volume for this hard sphere cell model reads $v_{\mathrm{free}}^{\mathrm{pl}}=[(\sqrt{2}/\rho)^{1/3}-2R_{\mathrm{mean}}]^3/\sqrt{2}$ and we obtain for the free energy in the plastic crystal phase

$$f_{\mathrm{pl}}=f^{\mathrm{rot}}(\alpha=0)-\ln(\Lambda^{-3}v_{\mathrm{free}}^{\mathrm{pl}})+C_s. \tag{8}$$

Again, we have corrected our theory by the same constant C_s.

3. AAA crystal

We describe the AAA structure by stacking two-dimensional triangular hard-sphere crystals on top of each other and stretching them in the stacking direction while fixing the ratio of the lattice constants to be $p+1$. The free volume cell for this structure is a hexagonal prism with the free volume v_{free}^{AAA}, which is given in Appendix A. The free energy finally reads

$$f_{AAA}(\alpha)=f^{\mathrm{rot}}(\alpha)-\ln(\Lambda^{-3}v_{\mathrm{free}}^{AAA})+C_s. \tag{9}$$

Again, a final minimization with respect to the width of the orientation distribution is required and consistently the constant C_s is added.

4. bcc crystal

Contrary to the previously mentioned crystalline structures the bcc solid is built up by layers, where the oriented particles are located on a squared lattice perpendicular to the director. This structure is known only to be metastable for hard spheres; however, as we are also interested in the HSC

system as a basis for a perturbation theory for long-range potentials, we also consider this structure.

By a suitable stretching with a factor $p+1$ of the corresponding bcc hard-sphere crystal we obtain the anisotropic structure for HSCs. The free volume cell of the stretched bcc crystal is assumed to be the same as the one in the case of hard spheres, namely, a truncated octahedron with the free volume $v_{\rm free}^{\rm bcc}$; see Appendix A. The free energy from our cell theory including the constant C_s is

$$f_{\rm bcc}(\alpha)=f^{\rm rot}(\alpha)-\ln(\Lambda^{-3}v_{\rm free}^{\rm bcc})+C_s. \tag{10}$$

5. Columnar phase

The present approach is readily generalized to a columnar phase where aligned particles are fluidlike along tubes, which form a two-dimensional hexagonal lattice in the plane perpendicular to the director. However, in contrast to the computer simulation, the columnar phase will win always against the *AAA* crystal since a one-dimensional hard-rod system will never freeze [34]. This deficiency was recovered also in the theory for oriented cylinders [28]. For this reason our theory overestimates the stability of the columnar phase. In order to circumvent this problem we have discarded the columnar phase altogether.

6. Smectic-A phase

In the smectic phase the particles are oriented and arranged in layers perpendicular to the director. Within these layers the particles behave in fluidlike fashion. For the two-dimensional fluid of effective particles with diameter D^* we use a scaled particle description [35] to obtain the free energy

$$f_{\rm 2D}^{\rm spat}=\ln(\Lambda^2\rho_{\rm 2D})+\frac{2\eta_{\rm 2D}^*-1}{1-\eta_{\rm 2D}^*}-\ln(1-\eta_{\rm 2D}^*), \tag{11}$$

where $\eta_{\rm 2D}^*=\rho d\pi D^{*2}/4$ is the two-dimensional packing fraction of the effective hard disks and d the spacing between the smectic layers. In the remaining dimension we calculate the free energy from a one-dimensional cell model

$$f_{\rm 1D}^{\rm spat}=-\ln(\Lambda^{-1}v_{\rm free}^{\rm sm}),$$

with the free volume $v_{\rm free}^{\rm sm}=d-(D^*+L^*)$.

The total free energy then reads

$$f_{\rm sm}(\alpha,d)=f^{\rm rot}(\alpha)+f_{\rm 1D}^{\rm spat}(\alpha,d)+f_{\rm 2D}^{\rm spat}(\alpha,d)+C_s/3. \tag{12}$$

Consistent with the treatment of the crystalline structures, we add a third of the constant C_s to the free energy in the smectic phase as the system is solidlike in only one dimension. For $d\to D^*+L^*$ the free energy $f_{\rm 1D}^{\rm spat}$ diverges. On the other hand, when $d\to 4/\rho\pi D^{*2}$ the term $f_{\rm 2D}^{\rm spat}$ goes to infinity. Consequently there is a minimum of the free energy $f_{\rm sm}(\alpha,d)$ for intermediate layer spacings. We finally minimize the free energy numerically with respect to the orientation distribution and the layer spacing.

7. Nematic phase

In the nematic phase all the particles are pointing by preference along the nematic director $\vec{\omega}_0$ while the center-of-mass coordinate shows no order. We approximate the free energy of this phase by considering a fluid of parallel hard spherocylinders with an effective diameter D^* and an effective length L^*. The scaled particle expression for the excess free energy of parallel hard spherocylinders reads [36]

$$f_{\rm nem}^{\rm ex}=\frac{3\eta^*-\eta^{*2}(3/2+B^2/6)}{(1-\eta^*)^2}-\ln(1-\eta^*), \tag{13}$$

with $B=\rho\pi L^*D^{*2}/4$. The packing fraction of the effective parallel hard spherocylinders was denoted by $\eta^*=\rho v_0^*$, with $v_0^*=\pi(D^{*3}/6+D^{*2}L^*/4)$ being the volume of the effective spherocylinder. To optimize the mapping we finally minimize

$$\tilde{f}_{\rm nem}(\alpha)=f^{\rm rot}(\alpha)+f^{\rm id}+f_{\rm nem}^{\rm ex}(\alpha) \tag{14}$$

with respect to the width of the orientation distribution (2). In order to compensate for the lack of configurations due to this crude mapping description we add a second empirical fitting parameter $C_n=-2.25$ to the free energy per particle. The value of this constant settles the isotropic-nematic-smectic as well as the isotropic-nematic-solid triple point and was chosen in comparison with computer simulations [14]. Hence the free energy of the nematic phase reads finally $f_{\rm nem}=\tilde{f}_{\rm nem}+C_n$.

8. Isotropic phase

In the isotropic (fluid) phase the excess free energy per particle is given within the scaled particle theory [26] as

$$f_{\rm iso}^{\rm ex}=\frac{a\eta+(a^2/6-a)\eta^2}{(1-\eta)^2}-\ln(1-\eta), \tag{15}$$

with

$$a=\frac{3(1+p)(1+p/2)}{1+(3/2)p}. \tag{16}$$

In the hard-sphere limit this expression corresponds to the Percus-Yevick approximation [37]. Here $\eta=\rho v_0$ is the volume fraction of the HSC with $v_0=\pi(D^3/6+LD^2/4)$ the volume of one HSC.

The remaining parts of the free energy are the contribution from the ideal rotators $f^{\rm rot}=1/4\pi$ and the ideal gas contribution $f^{\rm id}=\ln(\Lambda^3\rho)-1$. Thus the total free energy in the isotropic phase becomes

$$f^{\rm iso}=f^{\rm rot}+f^{\rm id}+f_{\rm iso}^{\rm ex}. \tag{17}$$

F. Results

The result of our theoretical description is shown in Fig. 2, where the phase behavior is shown as a function of the length-to-width ratio p and the reduced density ρ^*. The shaded areas correspond to the coexistence regions. Short rods freeze with increasing density first into a plastic crys-

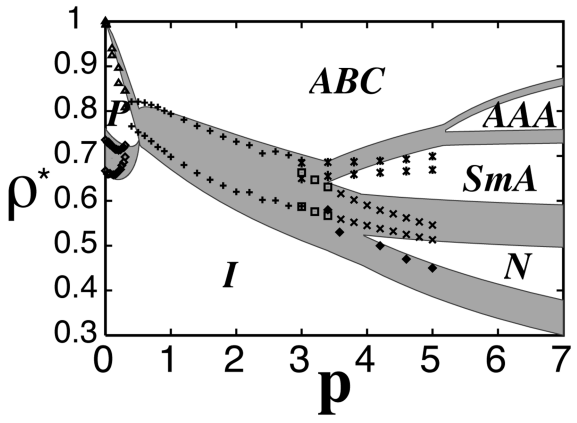

FIG. 2. Phase diagram for HSC in the ρ^*-p plane, where $\rho^* = \rho/\rho_{CP}$. The shaded area corresponds to the coexistence region calculated within the cell theory and the dots are the simulation data from Ref. [14]. There is an aligned AAA solid, an aligned ABC solid, a plastic crystal (P), an isotropic fluid (I), and a nematic (N) and a smectic-A (SmA) phase. The symbols for the simulational data are +, I-ABC transition; ◇, I-P transition; □, I-SmA transition; ◆, I-N transition; × N-SmA transition; *, SmA-ABC transition; ▲, P-ABC transition.

talline structure (P). For higher densities this plastic crystal then transforms into an orientationally ordered ABC crystal. Note that our theory respects the close-packed limit, i.e., the free energy diverges when approaching this structure. For length-to-width ratios larger than $p=0.522$ the plastic crystal becomes metastable and the isotropic fluid (I) directly freezes into the ordered solid. Beyond an aspect ratio of $p=3.4$ a smectic-A phase (SmA) becomes stable. For a slightly larger length-to-width ratio the isotropic fluid transforms first with increasing density into a nematic phase (N), then into a smectic-A phase, and finally into an ABC solid. Long HSCs with $p \geqslant 5.19$ first freeze into an AAA structure. The stretched bcc crystalline phase was never stable within our theory.

Comparison with the computer simulations of Bolhuis and Frenkel [14] shows good overall agreement. These data are included in Fig. 2 as dots. All stable phases and the topology of the phase diagram are remarkably well reproduced by our simple theory. Additionally, the theory reveals the correct slopes of all coexistence lines. However, one observes when comparing the results to simulational data that the theory shows some deviations for longer rods, e.g., the stability of the AAA structure is overestimated. Also, the isotropic-nematic transition in our theory does not respect the Onsager limit and density jumps are overestimated.

III. PERTURBATION THEORY FOR SOFT INTERACTIONS

A. Model for the interaction

In this section we illustrate how to treat the soft interactions between the TMVs by a thermodynamic perturbation theory. We describe the TMV as a stiff cylinder with a (physical) length $l_{TMV}=300$ nm and diameter $d_{TMV}=18$ nm [8]. Furthermore, since we are interested only in mesoscopic length scales we ignore the detailed molecular structure. In an aqueous solution protons dissociate from the surface proteins leading, at a pH of 7, to a line charge of $10-20$ e/nm in titration experiments. However, some of these charges recondense at the surface. As only the boundary value of the counterion charge density at the Wigner-Seitz cell is responsible for the pair interaction, the total charge has to be renormalized to a lower value when considering the pair interaction [38–40]. A total charge number of roughly $Z=300-500$ was able to reproduce the static structure factor of light scattering experiments [41,42]. Here we thus take a fixed value of $Z=390$ for the total effective rod charge.

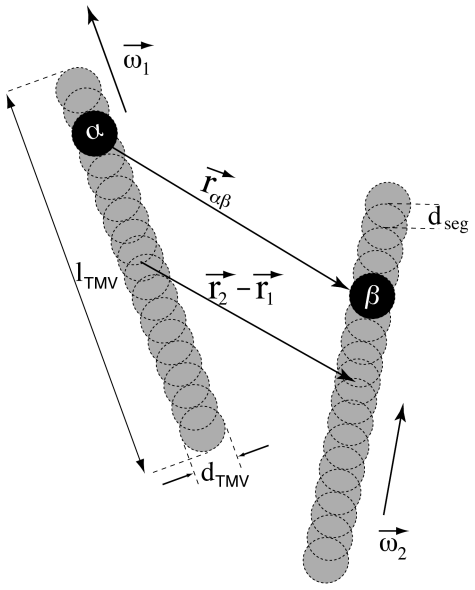

FIG. 3. Yukawa-segment model for the pair interaction of two charged rods The physical parameters are the length l_{TMV} and the width d_{TMV} of the virus particles. We model the pair interaction of two rods pointing in the $\vec{\omega}_1$ and $\vec{\omega}_2$ directions and being a distance $\vec{r}_1-\vec{r}_2$ apart by a Yukawa-segment model. There are $N_s=17$ beads in a distance d_{seg} aligned on the rods and their mutual distance is $|\vec{r}_{\alpha\beta}|$.

By density functional perturbation theory it was recently demonstrated how to obtain the effective Derjaguin-Landau-Verwey-Overbeek pair interaction within the primitive model [43,16,44]. By this derivation, additional ''volume terms'' show up, which shift the phase boundaries particularly for salt-free suspensions. Although these studies are done for spherical macro-ions, a similar derivation is possible for rodlike macro-ions [45] where the charge is distributed on segmentlike beads along the rods.

Still the rods retain a (physical) spherocylindric hard core. The total pair interaction between rods possessing orientations $\vec{\omega}_1$ and $\vec{\omega}_2$ and a center-of-mass difference vector $\vec{r}_2-\vec{r}_1$ reads

$$u(\vec{r}_2-\vec{r}_1,\vec{\omega}_1,\vec{\omega}_2) = \begin{cases} \infty & \text{if the physical hard cores overlap} \\ \dfrac{(Ze/N_s)^2}{\epsilon}\displaystyle\sum_{\alpha,\beta=1}^{N_s}\dfrac{\exp[-\kappa r_{\alpha\beta}]}{r_{\alpha\beta}} & \text{otherwise.} \end{cases} \tag{18}$$

Here the sum runs over N_s beads labeled α and β, which have a distance $|\vec{r}_{\alpha\beta}|$ (see Fig. 3). Each of these beads carries a charge Z/N_s; ϵ is the dielectric constant of the solvent-.The segments are arranged in such a spacing $d_{\rm seg}$ that the quadrupole moments of the uniformly charged rod and the segment rod are identical, which leads to

$$d_{\rm seg}=\frac{l_{\rm TMV}}{\sqrt{(N_s-1)(N_s+1)}}. \tag{19}$$

Two contributions enter into the inverse Debye screening length

$$\kappa=\sqrt{\frac{4\pi e^2}{\epsilon k_B T}(Z\rho+2n_s)}, \tag{20}$$

namely, the density of the counterions stemming from the macroparticles $Z\rho$, and the salt concentration n_s. In Eq. (20) k_BT is the thermal energy and $\rho=N/V$ the rod density.

B. Splitting the potential and treatment of the reference system

The key idea of perturbation theory is to separate the dominant behavior of the pair interaction and to treat the remaining part as a perturbation. The free energy splits into a reference part $\mathcal{F}_0$ and a term describing the perturbation $\mathcal{F}^{\rm pert}$ as

$$\mathcal{F}=\mathcal{F}_0+\mathcal{F}^{\rm pert}. \tag{21}$$

As a reference system we take hard spherocylinders with an *effective* size, namely, an effective diameter $d_{\rm eff}$ and an effective length $l_{\rm eff}$. These effective sizes for the hard body instead of the physical ones take into account the slow decay of the potential in the case of low added salt.

To obtain these effective sizes we make use of a simple generalization of the scheme proposed by Kang *et al.* [46]. First we define a typical in-plane distance r_0 between parallel oriented rods by putting all particles on a distorted fcc lattice. At this splitting range

$$r_0=[\sqrt{2}/(\rho l_{\rm TMV}/d_{\rm TMV})]^{1/3} \tag{22}$$

we then split the two-dimensional potential of two parallel in-plane rods into a short-range part $u_0^{\rm 2D}(r)$ and a long-range part $w^{\rm 2D}(r)$ such that $u^{\rm 2D}(r)=u_0^{\rm 2D}(r)+w^{\rm 2D}(r)$. In particular,

$$u_0^{\rm 2D}(r)=\begin{cases} u^{\rm 2D}(r)-G(r) & \text{for } r\leqslant r_0 \\ 0 & \text{otherwise,}\end{cases} \tag{23}$$

$$w^{\rm 2D}(r)=\begin{cases} G(r) & \text{for } r\leqslant r_0 \\ u^{\rm 2D}(r) & \text{otherwise,}\end{cases} \tag{24}$$

where the linear function

$$G(r)=u^{\rm 2D}(r_0)-\left.\frac{du^{\rm 2D}(r)}{dr}\right|_{r=r_0}(r_0-r) \tag{25}$$

guarantees continuity of $u^{\rm 2D}(r)$ and $w^{\rm 2D}(r)$ and their derivatives at $r=r_0$. We now use the short-range potential to construct an effective (two-dimensional) diameter by applying the Barker-Henderson formula [47]

$$d_{\rm eff}=\int_0^\infty [1-e^{-\beta u_0^{\rm 2D}(r)}]dr, \tag{26}$$

while the effective length for the HSC reference system is given by $l_{\rm eff}=(N_s-1)d_{\rm seg}$.

C. Treatment of the long-range perturbation

The remaining perturbation is treated in a mean-field fashion. In particular, we split the full pair potential as $u(\mathbf{x}_1,\mathbf{x}_2)=u_0(\mathbf{x}_1,\mathbf{x}_2)+w(\mathbf{x}_1,\mathbf{x}_2)$, where $\mathbf{x}\equiv(\vec{r},\vec{\omega})$. The potential $u_\lambda=u_0+\lambda w$ interpolates, by the parameter $\lambda\in[0,1]$, between the reference potential u_0 and the full potential by adding the perturbation w.

By thermodynamic integration one obtains the exact relation [37] for the total free energy $\mathcal{F}$,

$$\begin{aligned}\mathcal{F}&=\mathcal{F}_0+\mathcal{F}^{\rm pert}\\ &=\mathcal{F}_0+\frac{1}{2}\int_0^1 d\lambda\int\int\rho_\lambda^{(2)}(\mathbf{x}_1,\mathbf{x}_2)w(\mathbf{x}_1,\mathbf{x}_2)d\mathbf{x}_1d\mathbf{x}_2.\end{aligned} \tag{27}$$

$\mathcal{F}_0$ denotes the HSC reference free energy, which is approximately known in the different liquid-crystalline phases from Sec. III B. $\rho_\lambda^{(2)}(\mathbf{x}_1,\mathbf{x}_2)$ is the two-particle density for the potential $u_\lambda(\mathbf{x}_1,\mathbf{x}_2)$ in the different phases.

To evaluate the perturbative part of the free energy $\mathcal{F}^{\rm pert}$ the pair interaction is split on the level of the single beads by using the same (scaled) support function $G(r)$ from the two-dimensional case. We thus approximate the short- and long-range potentials for the rods with an orientational degree of freedom by

$$\begin{aligned}&u_0(\vec{r}_{12},\vec{\omega}_1,\vec{\omega}_2)\\ &\quad=\sum_{\alpha,\beta=1}^{N_s}\times\begin{cases}\dfrac{(Ze/N_s)^2}{\epsilon}\dfrac{e^{-\kappa r_{\alpha\beta}}}{r_{\alpha\beta}}-\dfrac{G(r_{\alpha\beta})}{N_s^2} & \text{for } r_{\alpha\beta}\leqslant r_0\\ 0 \quad \text{otherwise,}\end{cases}\end{aligned} \tag{28}$$

$$w(\vec{r}_{12},\vec{\omega}_1,\vec{\omega}_2)=\sum_{\alpha,\beta=1}^{N_s}\times\begin{cases}\dfrac{G(r_{\alpha\beta})}{N_s^2} & \text{for } r_{\alpha\beta}\leqslant r_0\\ \dfrac{(Ze/N_s)^2}{\epsilon}\dfrac{e^{-\kappa r_{\alpha\beta}}}{r_{\alpha\beta}} & \text{otherwise.}\end{cases} \tag{29}$$

D. Treatment of the different phases

As already explained, the free energy of the reference system is described within our cell theory from Sec. II. The reference system also fixes any variational parameters such as the width α^* of the orientation distribution and, for the smectic phase, the layer spacing d^*. In the spirit of first-order perturbation theory, these parameters will be kept unchanged to evaluate the perturbative part.

1. Isotropic phase

Here the particle density is uniform $\rho_{\rm iso}(\mathbf{x})=\rho_{\rm iso}=\rho/4\pi$. We use a high-temperature approximation to the pair distribution function, obtaining

$$\rho_\lambda^{(2)}(\mathbf{x}_1,\mathbf{x}_2)=\rho_{\rm iso}(\mathbf{x}_1)\ \ \rho_{\rm iso}(\mathbf{x}_2)\ \ e^{-\beta u_\lambda(\mathbf{x}_1,\mathbf{x}_2)}. \tag{30}$$

Doing the final integration over λ one gets

$$\begin{aligned}\mathcal{F}^{\rm pert}&=\frac{1}{2}k_BT\int\int d\mathbf{x}_1d\mathbf{x}_2\rho_{\rm iso}(\mathbf{x}_1)\rho_{\rm iso}(\mathbf{x}_2)\\&\quad\times e^{-\beta u_0(\mathbf{x}_1,\mathbf{x}_2)}[1-e^{-\beta w(\mathbf{x}_1,\mathbf{x}_2)}]\\&\approx\frac{1}{2}\int\int d\mathbf{x}_1d\mathbf{x}_2\rho_{\rm iso}(\mathbf{x}_1)\rho_{\rm iso}(\mathbf{x}_2)e^{-\beta u_0(\mathbf{x}_1,\mathbf{x}_2)}w(\mathbf{x}_1,\mathbf{x}_2),\end{aligned} \tag{31}$$

where we again made a high-temperature approximation.

It is convenient to expand the expression $h(\vec{r},\vec{\omega}_1,\vec{\omega}_2)\equiv e^{-\beta u_0(\vec{r},\vec{\omega}_1,\vec{\omega}_2)}w(\vec{r},\vec{\omega}_1,\vec{\omega}_2)$ from Eq. (31) into spherical invariants:

$$h(\vec{r},\vec{\omega}_1,\vec{\omega}_2)=\sum_\Lambda\hat{h}_\Lambda(r)\Phi_\Lambda(\vec{\omega}_{12},\vec{\omega}_1,\vec{\omega}_2). \tag{32}$$

Due to the symmetric properties, the summation runs only over the multidimensional index $\Lambda=(l,l_1,l_2)$, involving only even l,l_1,l_2. The derivation of the expansion coefficients $\hat{h}_\Lambda$ can be found in Appendix B. This simplifies the expression (31) further to

$$\mathcal{F}_{\rm iso}^{\rm pert}=\frac{N}{2}\rho\frac{1}{\sqrt{4\pi}}\int_0^\infty dr\,r^2\hat{h}_{000}(r). \tag{33}$$

2. Nematic phase

For the perturbative part we start with the one-particle density $\rho_{\rm nem}(\mathbf{x})=\rho,g(\vec{\omega};\alpha^*)$, where the width of the orientation distribution α^* was already fixed by the reference system of the effective HSC. Approximating again the pair distribution function by a low-density expression (30), the perturbation contribution is similar to the isotropic case (31). Expanded into spherical harmonics, this yields

$$\begin{aligned}\mathcal{F}_{\rm nem}^{\rm pert}=\frac{N}{2}\rho\frac{1}{\sqrt{4\pi}}\sum_{l\ \rm even}\sqrt{2l+1}\int dr\,r^2\hat{h}_{ll0}(r)\\\times\left[\int g(\vec{\omega};\alpha^*)P_l(\vec{\omega}\cdot\vec{\omega}_0)d^2\vec{\omega}\right]^2,\end{aligned} \tag{34}$$

where $P_l(x)$ is the lth Legendre polynomial.

3. Smectic phase

We approximate the one-particle density by

$$\rho_{\rm sm}(\mathbf{x})=\rho^{\rm 2D}\sum_n\ \ \delta(r_z-nd^*)\ \ \ g(\vec{\omega};\alpha^*), \tag{35}$$

describing a homogeneous fluid of particles exactly confined in layers a distance d^* apart. In Eq. (35) the spatial coordinate perpendicular to the layers is denoted by r_z and $\rho^{\rm 2D}=\rho d^*$ is the effective two-dimensional density.

The two-particle density is further approximated by

$$\begin{aligned}\rho^{(2)}(\mathbf{x}_1,\mathbf{x}_2)=(\rho^{\rm 2D})^2\Bigg(\sum_n\ \delta(r_{z_1}-nd^*)\\\times\delta(r_{z_2}-nd^*)g_0(\vec{r}_1,\vec{r}_2)\\+\sum_{n,n'}\ \delta(r_{z_1}-nd^*)\,\delta(r_{z_2}-n'd^*)\Bigg)\\\times g(\vec{\omega}_1,\alpha^*)g(\vec{\omega}_2,\alpha^*).\end{aligned} \tag{36}$$

Here $g_0(\vec{r}_1,\vec{r}_2)$ is the pair distribution function of the center-of-mass coordinates of two hard spherocylinders in the reference system.

The perturbative part of the free energy (27) thus splits as

$$\mathcal{F}_{\rm sm}^{\rm pert}=\mathcal{F}_{\rm sm}^{\rm pert,\ 1D}+\mathcal{F}_{\rm sm}^{\rm pert,\ 2D}. \tag{37}$$

By using Eqs. (27), (36), and (37) the two-dimensional fluidlike expression reads

$$\mathcal{F}_{\rm sm}^{\rm pert,\ 2D}=\frac{N}{2}\rho^{\rm 2D}\int_{\sigma_{\rm 2D}}^\infty d^2r\,g^{\rm 2D}(r)\ \ \tilde{w}^{\rm 2D}(r;\alpha^*), \tag{38}$$

where we introduced the (two-dimensional) hard-disk pair distribution function $g^{\rm 2D}(r)$, which is obtained from $g_0(\vec{r}_2-\vec{r}_1)$ via

$$g^{\rm 2D}(r)=g_0(\sqrt{r_x^2+r_y^2})\equiv\int dr_z g_0(\vec{r})\,\delta(r_z). \tag{39}$$

Here $\vec{r}=(r_x,r_y,r_z)$. In the calculations we use an approximate density expansion for $g^{\rm 2D}(r)$, which is valid for area fractions up to $\approx O(0.4)$ [48]. Furthermore, in Eq. (38) we defined, starting from the orientationally averaged long-range potential

$$\begin{aligned}\tilde{w}(\vec{r}_2-\vec{r}_1;\alpha^*)=\int d^2\vec{\omega}_1\int d^2\vec{\omega}_2 g(\vec{\omega}_1,\alpha^*)\\\times g(\vec{\omega}_2,\alpha^*)w(\mathbf{x}_1,\mathbf{x}_2),\end{aligned} \tag{40}$$

a two-dimensional equivalent by

$$\tilde{w}^{\rm 2D}(r;\alpha^*)=\int dr_z\delta(r_z)\tilde{w}(\vec{r};\alpha^*), \tag{41}$$

with $r=\sqrt{r_x^2+r_y^2}$.

The mean-field part in the remaining solidlike dimension is a lattice sum

$$\mathcal{F}_{\rm sm}^{\rm pert,\ 1D}=\frac{N}{2}\sum_n\ \tilde{w}^{\rm lay}(nd^*;\alpha^*), \tag{42}$$

with the in-layer averaged potential $\tilde{w}^{\rm lay}(r_z;\alpha^*) = \rho^{\rm 2D}\int dr_x \int dr_y \tilde{w}(\vec{r};\alpha^*)$. The summation in Eq. (42) accounts for the distinct layers.

4. ABC solid

As for the distinct layers in the smectic phase, we assume the particles in the perturbative part of the solid free energy to be exactly localized at their lattice positions $\vec{R}_i$:

$$\rho_{ABC}(\mathbf{x}) = \sum_{\vec{R}_i} \delta(\vec{r}-\vec{R}_i) g(\vec{\omega};\alpha^*). \tag{43}$$

Most of the structural information is contained in the one-particle densities. The two-particle density is thus given by

$$\rho^{(2)}(\mathbf{x}_1,\mathbf{x}_2) = \sum_{\vec{R}_i,\vec{R}_j} \delta(\vec{r}_1-\vec{R}_i)\,\delta(\vec{r}_2-\vec{R}_j) \times g(\vec{\omega}_1;\alpha^*) g(\vec{\omega}_2;\alpha^*). \tag{44}$$

The mean-field contribution (27) then reads

$$\mathcal{F}^{\rm pert}_{ABC} = \frac{N}{2} \sum_{\vec{R}_i} \tilde{w}(\vec{R}_i;\alpha^*), \tag{45}$$

summing over the lattice points of the distorted fcc lattice.

5. AAA solid

As for the ABC solid one has

$$\mathcal{F}^{\rm pert}_{AAA} = \frac{N}{2} \sum_{\vec{R}_i} \tilde{w}(\vec{R}_i;\alpha^*), \tag{46}$$

where the summation runs now over the lattice positions of an AAA structure.

E. Inclusion of the volume terms

The volume terms depend on the thermodynamic parameters, but are assumed to be independent of the phase. In detail, they read as [16,17]

$$F^{\rm vol} = F^0_+ + F^0_- + F^1, \tag{47}$$

with

$$F^0_+ = N_+ k_B T[\ln(\Lambda_+^3 \overline{\rho}_+) - 1], \tag{48}$$

$$F^0_- = N_- k_B T[\ln(\Lambda_-^3 \overline{\rho}_-) - 1], \tag{49}$$

$$F^1 = -\frac{1}{2}\left[N_m \frac{Z^2 e^2}{\epsilon} \frac{\kappa}{N_s(1+\kappa d_{\rm TMV}/2)} + k_B T(N_+ - N_-)\left(\frac{\overline{\rho}_+ - \overline{\rho}_-}{\overline{\rho}_+ + \overline{\rho}_-}\right)\right], \tag{50}$$

where N_+ (ρ_+) and N_- (ρ_-) are the total number (density) of positive and negative micro-ions in the solution, i.e., $\rho_+ \equiv n_s + |Z|\rho$ and $\rho_- \equiv n_s$. Λ_+ and Λ_- denote the de Broglie wavelength of the positive and negative ions, respectively. A finite size correction [16] due to the physical core of the rods is included by considering it as a string of $N_s = 17$ spheres. To obtain phase equilibria we equate the total pressure and the chemical potential of the tobacco mosaic virus particles as well as the chemical potential of the negatively charged salt ions in coexistence.

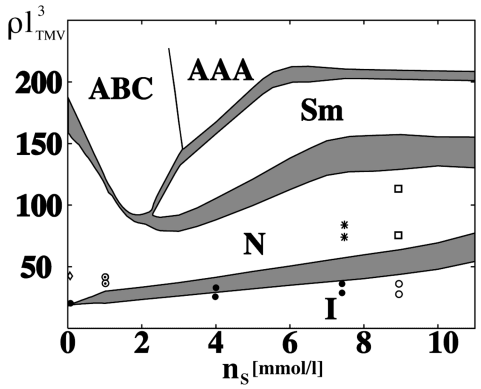

FIG. 4. Phase diagram of the tobacco mosaic virus. The coexistence densities in units of $1/l^3_{\rm TMV}$ are plotted versus the concentration n_s of added monovalent salt. We observe a cascade of liquid crystalline phases: In addition to the isotropic (I), nematic (N), and smectic-A(SmA) phases, two different colloidal crystalline structures, with an AAA and an ABC stacking, become stable. The experimental data are depicted as follows. ●, I-N coexistence densities from Fraden *et al.* [51]; ○, I-N coexistence densities and □, density values where a smectic-A phase is stable from Hirai *et al.* [54]; * smectic-A values reported by Wen *et al.* [6]; ♢, a colloidal crystalline structure for vanishing additional salt concentrations reported by Kreibig and Wetter [4] and Fraden *et al.* [5]. For a salt concentration of $1mM$ computer simulations for I-N coexistence densities are available [49] (⊙).

For high salt concentrations the volume terms can be neglected [17]. In order to speed up the phase coexistence calculations, we have included them only in the case $Z\rho > 2n_s$, i.e., when the number of ions stemming from the macro-ions is larger than the number of salt ions.

IV. RESULTS FOR THE PHASE DIAGRAM

The sample parameters we used are the usual ones for aqueous solutions (dielectric constant $\epsilon = 81$ at room temperature $T = 298$ K). For the number of sites, $N_s = 17$ was chosen. The resulting phase diagram is shown in Fig. 4. At high salt concentrations the typical sequence in the phase behavior of long hard rods is obtained: With increasing density the fluid transforms into a nematic, a smectic, and finally an AAA crystal. The close-packed structure, the ABC crystal, will become stable at very high densities out of the range considered here. Below a salt concentration of $n_s = 3.1mM$ the AAA structure is replaced by an ABC crystal. This is due to the reduction of the effective length-to-width ratio for decreasing salt concentration. Finally, below $n_s = 2.25mM$ the smectic phase becomes unstable.

Another interesting feature of the phase diagram is a *reentrant behavior of the nematic phase* for fixed density and increasing salt concentration ($\rho l^3_{\rm TMV} \approx 100$). The nematic phase is stable for strongly deionized samples. By increasing the salt concentration the system freezes into an ABC crys-

tal, which then transforms into a smectic phase. For even higher salt concentration, the system again gets into a nematic phase. This theoretical prediction can be verified in experiments. Still, we do not know at present whether the counterintuitive reentrant nematic phase is an artifact of our approximations.

We make three remarks about other possible phases. First, as our theory for the reference system overestimates the stability of a columnar phase, we do not consider this structure here. Second, the aspect ratio of our effective particles is always of order one and larger. Thus a plastic crystal will not be stable. Third, by explicit calculations, the stability of the cubic bcc structure was ruled out.

There is one special coexistence point of the *I-N* transition where computer simulation data are available [49], namely, for a salt concentration of $1mM$. The simulation was done for the same Yukawa-segment model and the same parameters we used in our theoretical calculations. The comparison with our theory is fair (see again Fig. 4), proving that our approximations for the isotropic and nematic phases are reasonable.

V. COMPARISON OF THEORY AND EXPERIMENT

The full phase behavior of pure monodisperse TMV samples is experimentally still unknown. A major difficulty is due to polydispersity of the particles: The TMV has a tendency to aggregate top on top and experimental samples can be spoiled by broken rods. An important caveat for the comparison with our theory is that coexistence data for the TMV are reported for various experimental conditions. Samples are suspended in different buffers at different values of the *p*H. There is no obvious reason why the bare charge of the macroparticles should remain unaffected, which was one of our basic assumptions for the effective interactions. Additionally, the ions in these buffers are not necessarily monovalent as we assumed in our calculations.

Let us now briefly summarize the experimental data available. As experiments on the *I-N* transition [1] had been performed on probably polydisperse systems, coexistence densities as a function of the ionic strength had been reexamined in detail by Fraden and co-workers [50,51,8,52], who explored the transition densities for many different salt concentrations. A crystalline structure in the absence of added salt had been explored. Oster [3] observed at low ionic strength a phase structured perpendicular to the director, i.e., either a smectic or a crystalline phase. Kreibig and Wetter [4] measured the layer spacing for these samples by light scattering. However, they observed a large variety of values stemming from different droplets within one sample. Fraden *et al.* [5] examined by x-ray scattering the structure within these layers and observed a crystalline structure, proving that for lowest ionic strengths a colloidal crystal is the stable structure. However, for extremely deionized samples evidence for a columnar phase has been claimed [7]. The structure of the samples with added salt was considered in various experiments. One observation was due to Kreibig and Wetter [4], who noted that the addition of salt destroys the liquid crystal in pure water irreversibly. Definite results for smectic phases had been reported by Meyer and co-workers [6,53]. The full range of virus particle concentrations for one fixed buffer concentration (10 mM sodium phosphate) was examined by Hirai *et al.* [54]. They reported the known sequence for long hard spherocylinders: isotropic, nematic, smectic-*A*, and precrystal phases. Even at the highest measured virus concentration, the structure within the layers remains only weakly ordered, implying that the full crystalline phase is not already obtained.

The experimental results are often given in terms of a calculated ionic strength, assuming a specific value of the virus particle charge. Thus we identify approximately equal ionic strengths of experimental samples with corresponding additional salt concentrations in our model and include in this way known experimental results to our phase diagram in Fig. 4. In particular, we reduced the experimental given ionic strength by the salt-free value and then assumed monovalent ions. Due to these caveats this data plot should only be understood as an attempt to make trends visible.

The increase of the coexistence densities of the isotropic-nematic transition with growing salt concentration is reproduced within our theory. Additionally, we observe a fully crystalline structure at vanishing salt concentration. Under these conditions a smectic phase is experimentally not observed, as within our theory. From the phase diagram it could also be explained that the colloidal crystal at vanishing additional salt concentrations could be transformed to more disordered structures by adding salt. Hence general trends are in good agreement with our theory, but a full quantitative comparison is not possible at the moment.

VI. CONCLUSION

In conclusion, we have presented a theory for the different liquid-crystalline phases for suspensions of TMV particles. The resulting phase diagram is quite rich, showing the stability of different phases including a reentrant nematic transition. It would be interesting to perform further computer simulations of our model in order to check quantitatively our theory for the phase diagram.

We finish with two remarks. First, experimental studies on the isotropic-nematic transition of rodlike colloidal particles in an *external alternating electric field* show a critical point [9]. This is a general feature between phases of the same spatial symmetry but with a different degree of orientational order. Thus, by external fields a critical point between the plastic solid and the *ABC*-stacked crystal might exist. It would be interesting to generalize our approach to such external fields coupling to the orientational degree of freedom. Second, a more microscopic theory is provided by the density functional approach of anisotropic particles. These theories, however, require a large numerical effort. Until now there had been no functional available, which generates the full phase behavior of HSCs. Still, some kind of weighted-density approximations [24] should be tested for the stability of the crystalline phases in order to get the full phase diagram. Our future work lies along these directions.

ACKNOWLEDGMENTS

We would like to thank M. Schmidt for helpful discussions. This work was supported by the DFG (Deutsche Forschungsgemeinschaft) within the Gerhard-Hess-Programm.

APPENDIX A: FREE VOLUME OF SOLID HSC PHASES

The basic assumption of our cell theory is that the HSCs have the same free volume cell as the corresponding hard-sphere crystal.

1. *ABC* solid

For the *ABC* solid the free volume cell is a rhombic dodecahedron. The free volume depends on the direction between two particles in two succeeding layers, measured with respect to the preference direction perpendicular to the layers $\theta_{\rm fcc}$, or, equivalently, on the angle in an equilateral pyramid, and is given by

$$v_{\rm free}^{ABC}=4\sqrt{2}y^3, \tag{A1}$$

with

$$y=a/2-\overline{R}(\pi/2,[g]),$$

$$a=-c+\frac{c^2}{b^{1/3}}+b^{1/3},$$

$$b=-2c^3+2\sqrt{2}/\rho+\sqrt{(2/\rho-4\sqrt{2}c^3)/\rho}\,,$$

$$c=\overline{R}(\theta_{\rm fcc},[g])-\overline{R}(\pi/2,[g]),$$

where $\overline{R}(\theta_{\rm fcc},[g])$ is defined in Eq. (4).

2. *AAA* solid

The shape of the free volume cell in an *AAA* crystal is a hexagonal prism. We fix the ratio of the long to short lattice constant to be equal to the full aspect ratio $x=p+1$. The free volume reads

$$v_{\rm free}^{AAA}=6\frac{a}{\sqrt{3}}\left(\frac{a}{2}-\overline{R}(\pi/2,[g])\right)^2\left(x-2\frac{\overline{R}(0,[g])}{a}\right), \tag{A2}$$

with

$$a=(2/\sqrt{3}\rho x)^{1/3}.$$

3. bcc solid

The free volume cell has the shape of a truncated octahedron and reads

$$v_{\rm free}^{\rm bcc}=4y^3, \tag{A3}$$

with

$$y=a/2-\overline{R}(\pi/2,[g]),$$

$$a=-c/3+\frac{c^2}{3b^{1/3}}+\frac{b^{1/3}}{3},$$

$$b=-c^3+27/\rho+3\sqrt{3}\sqrt{(27/\rho-2c^3)/\rho},$$

$$c=2\sqrt{6}\overline{R}(\theta_{\rm bcc},[g])-3\sqrt{2}\overline{R}(\pi/2,[g]).$$

APPENDIX B: EXPANSION IN SPHERICAL INVARIANTS

Here we anticipate the conventions of Gray and Gubbins [55]. The quantity $h(\vec{r},\vec{\omega}_1,\vec{\omega}_2)$ [Eq. (32)] depends on the unit vector $\vec{\omega}=\vec{r}/|\vec{r}|$. The rotational invariants

$$\Phi_\Lambda(\vec{\omega},\vec{\omega}_1,\vec{\omega}_2)=\sum_{m=-l}^{l}\sum_{m_1=-l_1}^{l_1}\sum_{m_2=-l_2}^{l_2}C(l_1l_2l,m_1m_2m)\times\mathcal{Y}_{l_1m_1}(\vec{\omega}_1)\mathcal{Y}_{l_2m_2}(\vec{\omega}_2)\mathcal{Y}^*_{lm}(\vec{\omega}), \tag{B1}$$

with $\mathcal{Y}_{lm}$ being spherical harmonics and $C(l_1l_2l,m_1m_2m)$ the Clebsch-Gordan coefficients, remain unchanged under simultaneous rotations of $\vec{\omega}_1,\vec{\omega}_2$, and $\vec{\omega}$. We expand therefore

$$h(\vec{r},\vec{\omega}_1,\vec{\omega}_2)=\sum_\Lambda \hat{h}_\Lambda(r)\Phi_\Lambda(\vec{\omega},\vec{\omega}_1,\vec{\omega}_2), \tag{B2}$$

where the summation is running over the triple $\Lambda=(l_1,l_2,l)\in\mathbb{N}_0^3$. The expansion coefficients read

$$\hat{h}_\Lambda(r)=\frac{4\pi}{2l+1}\int_{S_2}d^2\vec{\omega}_1\int_{S_2}d^2\vec{\omega}_2\quad h(r;\vec{\omega}_1,\vec{\omega}_2,\vec{\omega})\times\Phi^*_\Lambda(\vec{\omega},\vec{\omega}_1,\vec{\omega}_2). \tag{B3}$$

As they are rotationally invariant, we fix $\vec{\omega}$ pointing along the z axis, $\vec{\omega}=\hat{e}_z$, to calculate them. The expansion coefficients thus read, with $\overline{m}=-m$,

$$\hat{h}_\Lambda(r)=\sqrt{\frac{4\pi}{2l+1}}\int d^2\vec{\omega}_1\int d^2\vec{\omega}_2\times\sum_{m=-\min(l_1,l_2)}^{\min(l_1,l_2)}C(l_1l_2l;m\overline{m},0)\mathcal{Y}^*_{l_1m}(\vec{\omega}_1)\times\mathcal{Y}^*_{l_2\overline{m}}(\vec{\omega}_2)h(r,\vec{\omega}_1,\vec{\omega}_2;\vec{\omega}=\hat{e}_z). \tag{B4}$$

Using the invariance of $h(\vec{r},\vec{\omega}_1,\vec{\omega}_2)$ if one of the $\vec{\omega}$'s changes sign, only those expansion coefficients with even l_1,l_2,l are nonzero.

[1] F. C. Bawden, N. W. Pirie, J. D. Bernal, and I. Fankuchen, Nature (London) **138**, 1051 (1936).
[2] M. Wilkins, A. R. Stokes, W. E. Seeds, and G. Oster, Nature (London) **166**, 127 (1950).
[3] G. Oster, J. Gen. Physiol. **33**, 445 (1950).
[4] U. Kreibig and C. Wetter, Z. Naturforsch. C **35**, 751 (1980).
[5] S. Fraden, D. Caspar, and W. Philips, Biophys. J. **37**, 97a (1982).
[6] X. Wen, R. B. Meyer, and D. L. D. Caspar, Phys. Rev. Lett. **63**, 2760 (1989).
[7] M. Hagenbüchle, Ph.D. thesis, University Konstanz, 1993 (unpublished).
[8] S. Fraden, in *Observation, Prediction and Simulation of Phase Transitions in Complex Fluids*, edited by M. Baus, L. F. Rull, and J.-P. Ryckaert (Kluwer Academic, Dordrecht, 1995), p. 113.
[9] J. Tang and S. Fraden, Phys. Rev. Lett. **71**, 3509 (1993).
[10] Z. Dogic and S. Fraden, Phys. Rev. Lett. **78**, 2417 (1997).
[11] H. N. W. Lekkerkerker, P. Buining, J. Buitenhuis, and G. J. Vroege, in *Observation, Prediction and Simulation of Phase Transitions in Complex Fluids* (Ref. [8]), p. 53.
[12] P. A. Buining, A. P. Philipse, and H. N. W. Lekkerkerker, Langmuir **10**, 2106 (1994).
[13] L. Onsager, Ann. (N.Y.) Acad. Sci. **51**, 627 (1949).
[14] P. Bolhuis and D. Frenkel, J. Chem. Phys. **106**, 666 (1997).
[15] A. Stroobants, H. N. W. Lekkerkerker, and D. Frenkel, Phys. Rev. Lett. **57**, 1452 (1986).
[16] R. van Roij and J. P. Hansen, Phys. Rev. Lett. **79**, 3082 (1997).
[17] H. Graf, H. Löwen, and M. Schmidt, Prog. Colloid Polym. Sci. **104**, 177 (1997).
[18] J. Han and J. Herzfeld, in MRS Symposium Proceedings No. 463 (Materials Research Society, Pittsburgh, 1997), p. 135.
[19] J. A. C. Veerman and D. Frenkel, Phys. Rev. A **41**, 3237 (1990).
[20] D. Frenkel, H. N. W. Lekkerkerker, and A. Stroobants, Nature (London) **332**, 822 (1988).
[21] S. C. McGrother, D. C. Williamson, and G. Jackson, J. Chem. Phys. **104**, 6755 (1996).
[22] S.-D. Lee, J. Chem. Phys. **87**, 4972 (1987).
[23] A. M. Somoza and P. Tarazona, Phys. Rev. A **41**, 965 (1990).
[24] A. Poniewierski and R. Holyst, Phys. Rev. Lett. **61**, 2461 (1988).
[25] A. Poniewierski and T. J. Sluckin, Phys. Rev. A **43**, 6837 (1991).
[26] J. A. Barker and D. Henderson, Rev. Mod. Phys. **48**, 587 (1976).
[27] A. Ishihara and T. Hayashida, J. Phys. Soc. Jpn. **6**, 46 (1950).
[28] M. P. Taylor, R. Hentschke, and J. Herzfeld, Phys. Rev. Lett. **62**, 800 (1989).
[29] J. G. Kirkwood, J. Chem. Phys. **18**, 380 (1950).
[30] W. W. Wood, J. Chem. Phys. **20**, 1334 (1952).
[31] P. G. Bolhuis, D. Frenkel, S.-C. Mau, and D. A. Huse, Nature (London) **388**, 235 (1997).
[32] R. J. Speedy, J. Phys.: Condens. Matter **10**, 4387 (1998).
[33] M. Schmidt and H. Löwen, Phys. Rev. E **55**, 7228 (1997).
[34] L. Tonks, Phys. Rev. **50**, 955 (1936).
[35] M. Baus and J. Colot, Phys. Rev. A **36**, 3912 (1987).
[36] M. A. Cotter and D. E. Martiere, J. Chem. Phys. **52**, 1909 (1970).
[37] J. P. Hansen and I. R. McDonald, *Theory of Simple Liquids* (Academic, New York, 1986).
[38] S. Alexander, P. M. Chaikin, P. Grant, G. J. Morales, P. Pincus, and D. Hone, J. Chem. Phys. **80**, 5776 (1984).
[39] H. Löwen, Phys. Rev. Lett. **72**, 424 (1994).
[40] H. Löwen, J. Chem. Phys. **100**, 6738 (1994).
[41] E. E. Maier, R. Krause, M. Deggelmann, M. Hagenbüchle, and R. Weber, Macromolecules **25**, 1125 (1992).
[42] M. Deggelmann *et al.*, J. Phys. Chem. **98**, 364 (1994).
[43] H. Löwen, J. P. Hansen, and P. A. Madden, J. Chem. Phys. **98**, 3275 (1993).
[44] H. Graf and H. Löwen, Phys. Rev. E **57**, 5744 (1998).
[45] E. Canessa, B. D'Aguano, B. Weyerich, and R. Klein, Mol. Phys. **73**, 175 (1991).
[46] H. S. Kang, C. S. Lee, T. Ree, and F. H. Ree, J. Chem. Phys. **82**, 414 (1985).
[47] J. A. Barker and D. Henderson, J. Chem. Phys. **47**, 4714 (1967).
[48] D. G. Chae, F. H. Ree, and T. Ree, J. Chem. Phys. **50**, 1581 (1969).
[49] T. Kirchhoff (private communication).
[50] S. Fraden, G. Maret, D. Caspar, and R. B. Meyer, Phys. Rev. Lett. **63**, 2068 (1989).
[51] S. Fraden, G. Maret, and D. Caspar, Phys. Rev. E **48**, 2816 (1993).
[52] S. Fraden, A. J. Hurd, R. B. Meyer, M. Cahoon, and D. Caspar, J. Phys. Colloq. **46**, C3-85 (1985).
[53] R. B. Meyer, in *Dynamics and Patterns in Complex Fluids*, edited by A. Onuki and K. Kawasaki, Springer Proceedings in Physics Vol. 52 (Springer, Berlin, 1990).
[54] M. Hirai, S. Arai, T. Takizawa, and Y. Yabuki, Phys. Rev. B **55**, 3490 (1997).
[55] C. G. Gray and K. E. Gubbins, *Theory of Molecular Fluids, Volume 1: Fundamentals* (Clarendon, Oxford, 1984).